Supporting Information

Biomass-derived carbon sponges for use as sodium-ion capacitor electrodes

Sara Payá, Noel Díez,* Marta Sevilla*

Instituto de Ciencia y Tecnología del Carbono (INCAR), CSIC, Francisco Pintado Fe 26, 33011 Oviedo, Spain

Table S1. Electrochemical performance of state-of-the-art heteroatom-doped carbons as sodium stores.

Material	Capacity at 0.1 A g^{-1} (mAh g^{-1})	Capacity at 10 A g^{-1} (mAh g^{-1})	ICE (%)	Ref.
AGS-650	524	161	60	This work
3D N-doped carbon network	~ 240	123	38	[1]
N,S co-doped CNF	352	150	37	[2]
N-doped hierarchical porous hollow carbon spheres	300	107	44	[3]
N, O, P co-doped hierarchical porous carbon	312	72	40	[4]
N-doped carbon fibers	361	105	43	[5]
N/S-co-coped carbon nanoparticles	726	188	68	[6]
N, S co-doping hard carbon	250	102	<40	[7]
S-doped hard carbon	777	353	84	[8]
S-doped carbon nanosheets	548	133	58	[9]
S covalently linked TiO_2/C nanofiber	410	203	66	[10]
S/N doped 3D porous carbon nanosheets	392	138	33	[11]

1 D. Qiu, C. Yue, C. Qiu, L. Xian, M. Li, F. Wang and R. Yang, *Electrochim. Acta*, 2022, **405**, 139791.

2 Q. Yu, T. Dong, R. Qiu and H. Wang, *Mater. Res. Bull.*, 2021, **138**, 111211.

3 L. Liu, Y. Lu, S. Wang, Y. Ding, Y. Chen, D. Qiu, D. Wang, J. Niu, J. Zhang, X. Chen and H. Song, *J. Colloid Interface Sci.*, 2022, **620**, 24–34.

4 C. Wang, Q. Yu, N. Zhao, B. Li, W. Shen, F. Kang, Z. H. Huang and R. Lv, *J. Mater.*, 2022, **8**, 1149–1157.

5 R. Yan, E. Josef, H. Huang, K. Leus, M. Niederberger, J. P. Hofmann, R. Walczak, M. Antonietti and M. Oschatz, *Adv. Funct. Mater.*, , DOI:10.1002/adfm.201902858.

6 N. Diez, M. Sevilla and A. B. Fuertes, *Carbon N. Y.*, 2023, **201**, 1126–1136.

7 Q. Jin, K. Wang, P. Feng, Z. Zhang, S. Cheng and K. Jiang, *Energy Storage Mater.*, 2020, **27**, 43–50.

8 B. Wan, H. Zhang, S. Tang, S. Li, Y. Wang, D. Wen, M. Zhang and Z. Li, *Sustain. Energy Fuels*, 2022, **6**, 4338–4345.

9 G. Zhao, D. Yu, H. Zhang, F. Sun, J. Li, L. Zhu, L. Sun, M. Yu, F. Besenbacher and Y. Sun, *Nano Energy*, 2020, **67**, 104219.

10 T. Zhang, X. Shi, Z. Mao, C. Luo, G. Li, R. Wang, B. He, J. Jin, Y. Gong and H. Wang, *Electrochim. Acta*, 2021, **399**, 139377.

11 X. Hu, Y. Liu, J. Chen, L. Yi, H. Zhan and Z. Wen, *Adv. Energy Mater.*, 2019, **9**, 1–10.

Table S2. Values of oxygen content and electrical conductivity determined for the as-obtained microporous carbon and the post-treated material.

	O content (wt%)	**Electrical conductivity (S cm^{-1})**
As-obtained	5.84	0.95
AGA-850	3.63	3.03

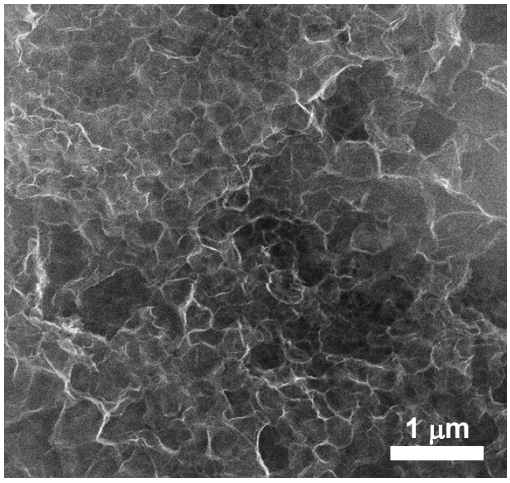

Figure S1. SEM micrograph of the non-doped material AG-600

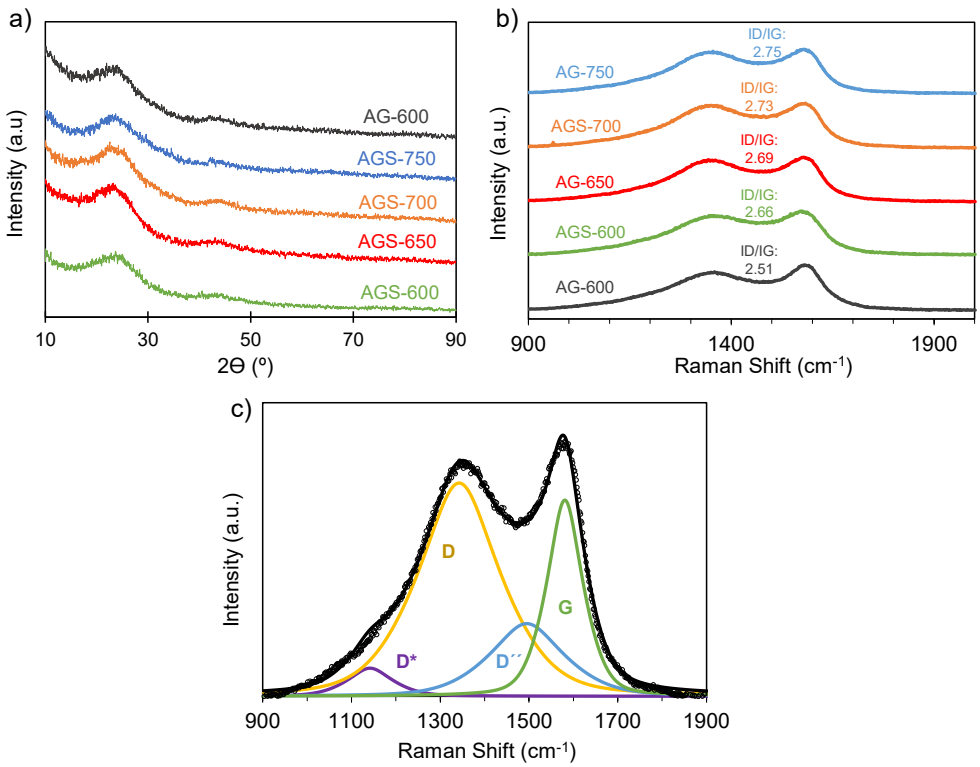

Figure S2. a) X-ray diffractograms and b) first-order Raman spectra of the S-doped carbon sponges and the non-doped material; c) example of deconvolution of the Raman spectrum of AGS-650 into four bands (D* ~1150 cm^{-1}, D ~1300 cm^{-1}, D´´ ~1500 cm^{-1} and G ~1600 cm^{-1}).

With increased doping temperature, there is a decrease of the heteroatom content and an increase of the electrical conductivity of the samples (Table 1), which points to a progressive ordering of the carbon structures. Accordingly, the increase of the I_D/I_G ratio observed with the rise of the doping temperature points to a decrease of defects according to the stage 2 of the three-stage Raman model proposed by Ferrari et al. (*Physical review B*, *61*(20), 14095).

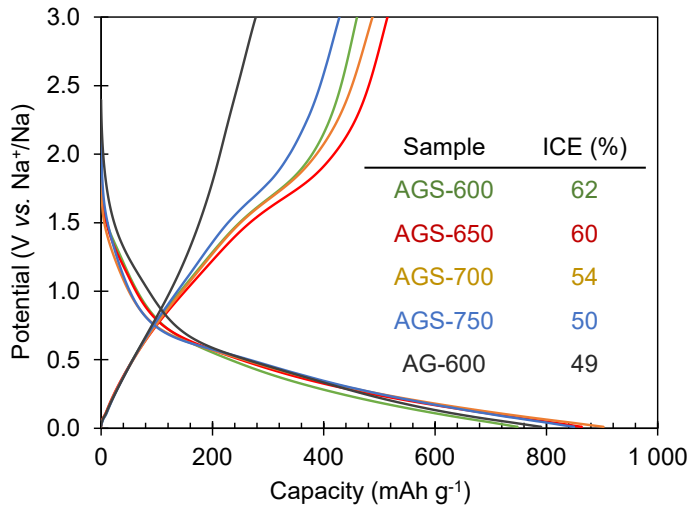

Figure S3. GCD profiles of the negative electrode materials corresponding to the first cycle recorded at 0.1 A g^{-1} (inset: ICE values).

a)

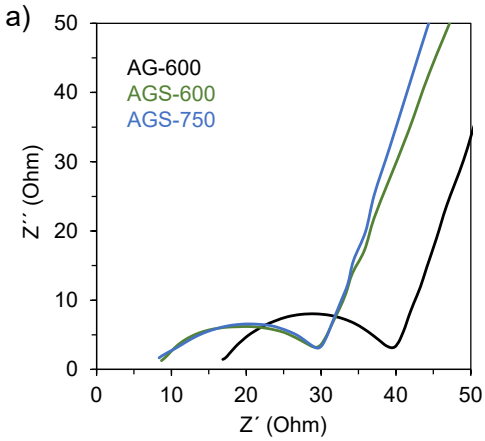

b)

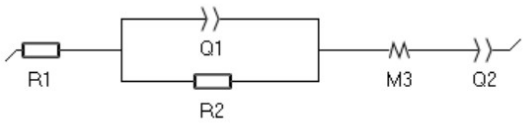

c)

	ESR (Ohm)	R_{ct} (Ohm)
AG-600	16.6	22.6
AGS-600	8.0	21.1
AGS-750	7.6	22.3

Figure S4. A) Nyquist plots of the cells recorded after the first sodiation-desodiation cycle; b) equivalent electric circuit model used for fitting the Nyquist plots and c) values of equivalent series resistance (ESR) and charge transfer resistance (R_{ct}) calculated based on this model.

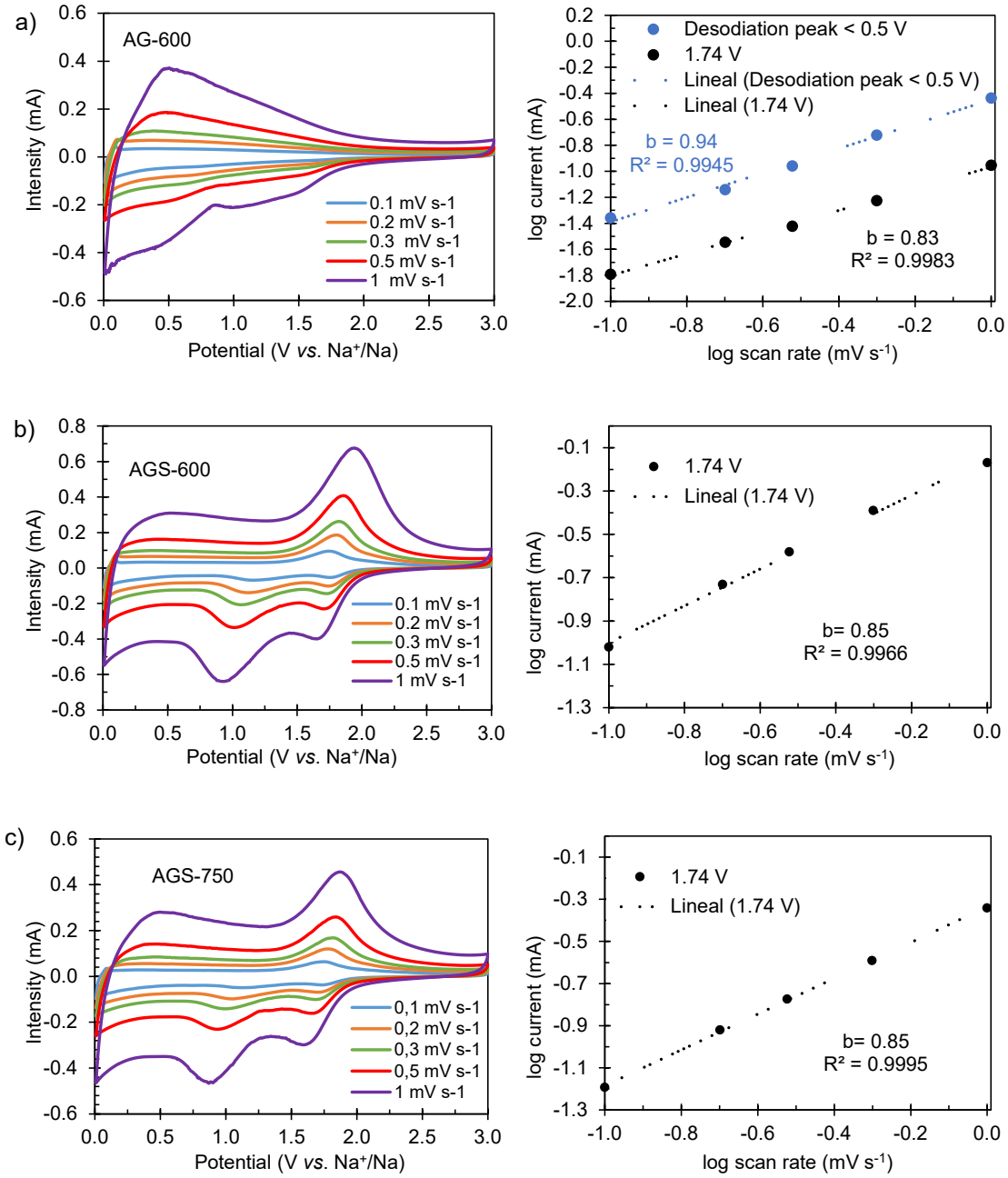

Figure S5. CVs recorded at different potential sweep rates (left) and determination of the *b* parameter at 1.74 V (right) for (a) AG-600, (b) AGS-600 and (c) AGS-750.

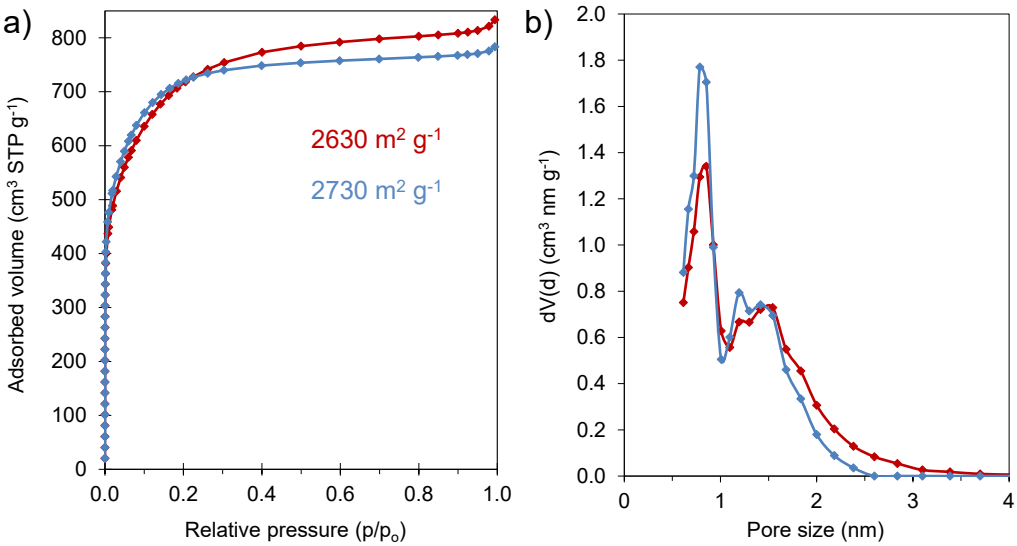

Figure S6. Nitrogen adsorption isotherm and pore size distribution corresponding to the microporous carbon before (blue) and after (red) the post-activation thermal treatment.

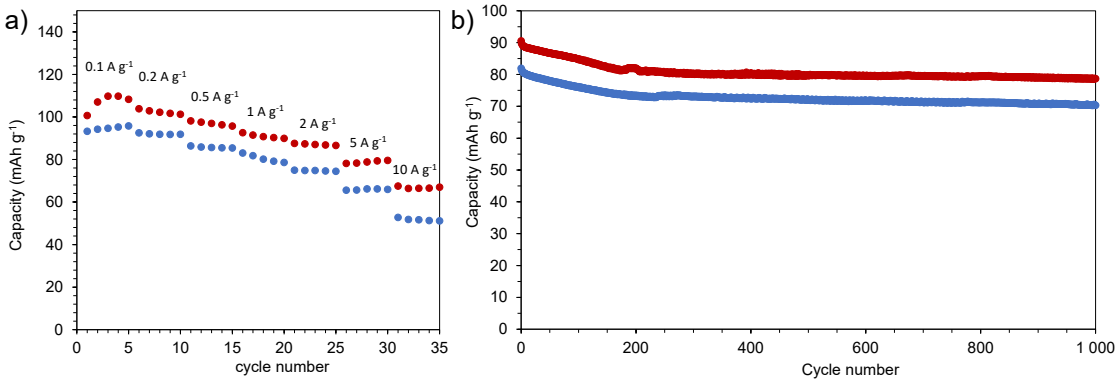

Figure S7. (a) Rate capability and (b) long term cycling stability test for the microporous carbon before (blue) and after (red) the post-activation thermal treatment.

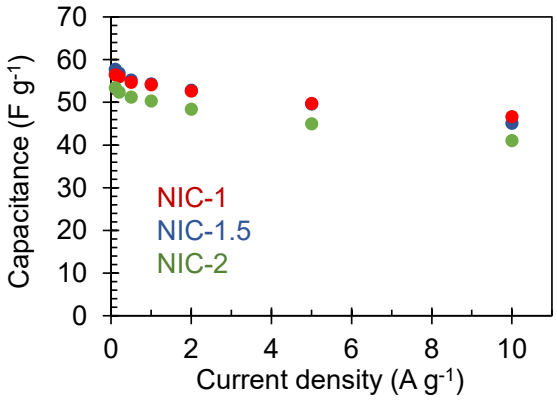

Figure S8. Rate capability of the full cells expressed in terms of capacitance.

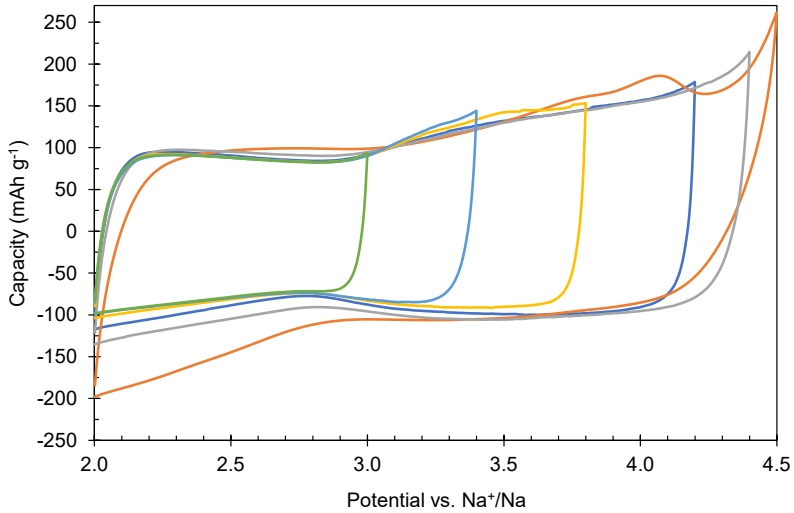

Figure S9. Cyclic voltammograms recorded for AGA-850 at increasing voltage window (potential sweep rate of 2 mV s^{-1}).

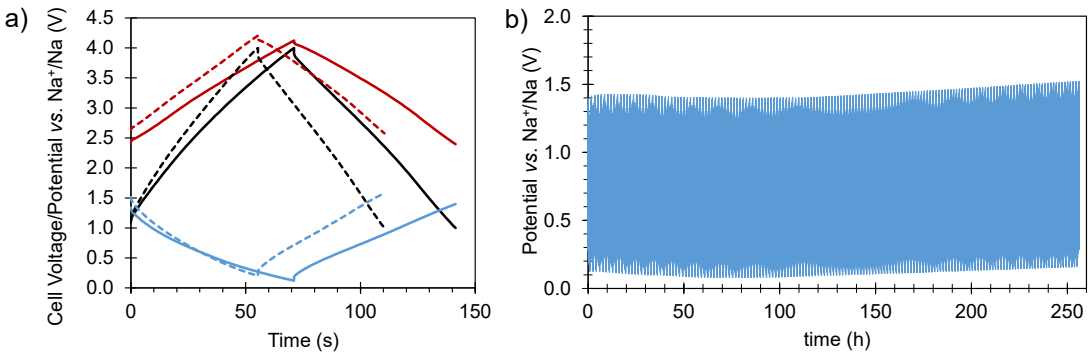

Figure S10. q) Cell voltage and electrode potential plots corresponding to the first (solid lines) and 10000th (dashed) cycles at 2 A g^{-1}; b) evolution of the negative electrode potential window during the whole cycling stability test.